Research Article

A Novel Interrupted-Sampling Repeater Jamming Suppression Method Based on Time-Frequency Analysis and Target Sparse Reconstruction

Zijian Wang [1,2] **Jiamu Li** [1,2] **Wenbo Yu** [1,2] **Yunhua Luo** [1] **and Zhongjun Yu** [1,2]

[1]*Aerospace Information Research Institute, Chinese Academy of Sciences, Beijing 100190, China*
[2]*School of Electronic, Electrical and Communication Engineering, University of Chinese Academy of Sciences, Beijing 101408, China*

Correspondence should be addressed to Zhongjun Yu; yuzj@ucas.ac.cn

Interrupted-sampling repeater jamming (ISRJ) is a new kind of coherent jamming for linear frequency modulation (LFM) signals. Based on digital radio frequency memory (DRFM), ISRJ can generate multiple false target groups by intercepting, storing, and retransmitting radar signal fragments, which significantly affects the postprocessing results of radar systems. Furthermore, due to the fragment interception of ISRJ, ISRJ false targets present a regular and discontinuous time-frequency (TF) distribution in contrast with real targets. Considering this intrinsic property and the coherent nature of ISRJ, this study proposes a new method based on TF analysis and target sparse reconstruction to address the ISRJ suppression issue. In this method, the echo signal is first sparsely represented to obtain both the real and false target positions. Then, according to the acquired target positions, information entropy features of targets are extracted in TF data for subsequent target identification. Finally, guided by the identification result, the real targets can be retained and reconstructed by adaptive filtering in the sparse domain to realize ISRJ suppression. Simulations have validated the effectiveness of the proposed method under various situations.

1. Introduction

Linear frequency modulation (LFM) signal is widely used in modern radar systems, and its large time-bandwidth product enables it to obtain a large coherent processing gain [1], which greatly mitigates the effect of noise jamming and other noncoherent jammings [2]. Therefore, coherent jamming is receiving increasing attention. With the widespread use of digital radio frequency memory (DRFM) in electronic countermeasures (ECM), many types of active coherent jammings have been developed. DRFM can coherently duplicate radar signals so that the transmission power requirement of jammers is lowered [3]. Meanwhile, DRFM is also characterized by adjustable jamming parameters and portability on different platforms, posing a severe threat to the radar system [4, 5].

There are two main working modes for DRFM-based jammers [6]. The first working mode is to intercept and forward the entire radar signal pulse, thus the generated jamming signal is able to obtain the coherent processing gain to the maximum extent and form a highly realistic deceptive target. Nevertheless, this kind of jamming cannot take effect until the next pulse repetition interval (PRI), so radar systems can adopt strategies such as interpulse waveform agility [7, 8], frequency agility [9, 10], and protecting signal [11] to counter such jamming. Besides, this working mode is restricted by the high isolation of two receive-and-transmit antennas and the sampling rate of the wideband signal, so it cannot be flexibly applied to small platforms such as missiles and unmanned aerial vehicles (UAVs) [12].

In order to solve the inherent defects of the first working mode, the other working mode named the interrupted-sampling-repeating mode came into being. In this mode,

interrupted-sampling repeater jamming (ISRJ) is proposed [13]. It intercepts, stores, and repeatedly forwards radar signals within a pulse duration and can generate a series of false targets after pulse compression (PC). The intrapulse jamming characteristic of ISRJ solves the application limitation of the first working mode and also invalidates the abovementioned jamming countermeasures. On this basis, scholars have further explored the application prospect and derivative forms of ISRJ [14–22]. In terms of specific application, the jamming theory and effect of ISRJ have been tested on various LFM wideband radars, such as PC radar [14], dechirping radar [15], and range doppler (RD) imaging radar [16–18]. In addition, Li et al. [19] quantify the influence of signal interception ratio on jamming power loss and evaluate the corresponding jamming effect. In the aspect of derived jamming types, Liu [20] proposes interrupted-sampling loop jamming (ISLJ) by changing the forwarding mode of intercepted radar signal fragments. In [21], ISRJ is combined with the scatter wave, and the jamming effect of resulting intermittent sampling scatter-wave jamming on SAR is verified. In [22], an improved ISRJ is proposed, which can generate false targets ahead of real targets by means of frequency shifting. However, the jamming thus formed may lead to an inevitable energy loss of the generated false targets.

On account of the practicality of ISRJ, the suppression methods against ISRJ have attracted extensive attention since ISRJ was proposed. These methods can be divided into waveform design methods and signal filtering methods. The waveform design methods divide the transmitted signal into multiple segments and then perform subpulse compression separately to destroy the intrapulse coherence of ISRJ as much as possible. For instance, Zhang et al. use a stepped LFM signal [23] and an intrapulse LFM-Costas frequency stepping signal [24] to increase the orthogonality among subpulses, thus the jammed subpulses can be easily eliminated through the energy threshold after subpulse compression. Similarly, a mixed modulation of frequency-shift keying (FSK)/phase-shift keying (PSK) signal is employed in [25] to distinguish the real targets from false ones via the accumulated target detection results after subpulse compression. In [26], guided by the estimated jamming parameters, Zhou et al. optimize the transmitted waveform by adopting protective pulses and genetic algorithms. Overall, the performance of the waveform design methods mainly depends on the orthogonality between the transmitted signal and ISRJ, and the energy loss of the real target increases when the jamming duty ratio becomes larger.

The signal filtering methods realize jamming removal by filtering in a certain transform domain. In these methods, one option is to extract the jamming-free radar signal fragments through energy function [27, 28], time-frequency (TF) function [29], and neural network [30]. This option, however, relies heavily on the intensity of the jamming signal and performs relatively poorly under weak jamming conditions. The other option is based on TF analysis. For the dechirping radar, a band-pass filtering process is carried out in the frequency domain [31, 32] by finding the TF local minimum value, but there are still some false targets remaining after processing. For the PC radar,

Zhou et al. estimate the key parameters of ISRJ [33] through TF analysis and deconvolution for jamming cancellation, and Meng et al. further adopt the Hilbert transform [34] to improve the estimation accuracy of ISRJ sampling slice width. Yet, the performance of these methods is sensitive to the parameter estimation accuracy [35, 36] and provides new ideas for jamming suppression. In [35], Lu et al. initially apply a TF mask to filter out the wideband jamming signal and then reconstruct the target signal according to the compressed sensing theory. In [36], the PC result is transformed into the TF domain, and a TF filter can be designed to filter out the false targets directly after determining the range gates of real targets. Nevertheless, this approach is limited by the contradiction between time resolution and frequency resolution in the TF transform, so it cannot accurately determine the extraction locations and the spectrum widths of the target range gates simultaneously. In [37], a new method for ISRJ suppression is proposed based on real target locating and recovery; the success rate of this method depends on the real target locating precision of the neural network. Although the method is limited to a single real target recovery, for the time being, it provides a new solution for ISRJ suppression.

In this context, according to the coherence of ISRJ and the different TF distribution characteristics between ISRJ false targets and real targets, this study proposes a new ISRJ suppression method for LFM PC radars based on TF analysis and target sparse reconstruction. This method converts the jamming suppression problem into a target binary classification problem, and the targets of interest can be recovered through sparse reconstruction assisted by the target identification result. Owing to the use of TF information entropy (TFIE) features, the proposed method can achieve an overall high target identification accuracy, and ISRJ false targets as well as the noise signal can be greatly suppressed after real target reconstruction. Furthermore, in the stage of TF feature extraction, the proposed method can locate the targets precisely by means of sparse representation and thus is free from the time resolution limit in the TF transform.

The structure of this study is as follows. Section 2 first introduces the ISRJ signal model and then analyzes the PC result of ISRJ and its corresponding TF distribution. Section 3 proposes the ISRJ suppression method, in which the procedures of target identification using TFIE and target sparse reconstruction are introduced in detail. Section 4 conducts lots of simulations to verify the effectiveness of the proposed method and also studies the factors affecting the antijamming probability. Finally, the main conclusions are drawn in Section 5.

2. Principle of ISRJ

2.1. ISRJ Signal Model.
ISRJ is mainly used for self-defensive purposes in defense penetration scenarios [28]. For the formation process of ISRJ, the jammer first intercepts and stores a fragment of the radar-transmitting signal and then forwards it repeatedly many times. This process is repeated till the end of the radar signal pulse, as shown in Figure 1.
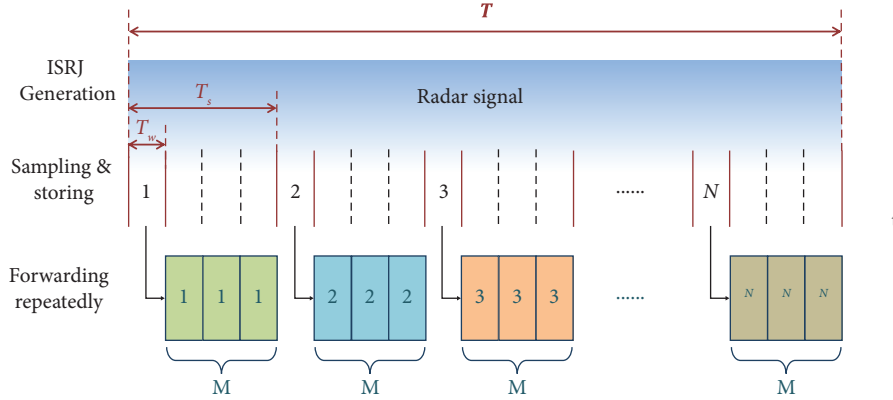
FIGURE 1: The formation process of ISRJ.

We assume that the radar transmits LFM signal $sig(t)$ with pulse width T and bandwidth B, and the distance between the radar and the real target is R_{tar}, then the target echo signal can be represented as

$$s_{tar}(t) = \sigma_{tar}\mathrm{sig}(t - \tau_{tar}) = \sigma_{tar}\mathrm{rect}\left(\frac{t - \tau_{tar}}{T}\right)e^{j\pi k(t - \tau_{tar})^2},$$

(1)

where $\mathrm{rect}(t/T)$ is a rectangular window function with window length T and starting point 0, σ_{tar} and $\tau_{tar} = 2R_{tar}/c$ represent the intensity and the propagation time delay of the target echo signal, respectively. $k = B/T$ is the frequency modulation rate of the LFM signal, and c is the speed of light.

As Figure 1 illustrates, the jammer samples the radar signal at a certain repeat sampling interval T_S within a signal pulse width, and the sampling slice width is T_W. Accordingly, the sampling function $p(t)$ can be defined as

$$p(t) = rect\left(\frac{t}{T_W}\right) \otimes \sum_{n=0}^{N-1} \delta(t - nT_S)$$

$$= \sum_{n=0}^{N-1} rect\left(\frac{t - nT_S}{T_W}\right),$$

(2)

where $\otimes$ denotes the convolution operator, $N = \lceil (T - T_W)/T_S \rceil$ is the number of sampled radar signal fragments [29, 30], and $\lceil \bullet \rceil$ is the round-up operator. Note that the relationship between the repeat sampling interval T_S and the sampling slice width T_W is $T_S = (M + 1)T_W$, in which M is the forwarding time of a jamming slice.

Therefore, the radar signal fragments sampled and stored by the jammer can be obtained as

$$s_{sam}(t) = \mathrm{sig}(t - \tau_{tar})p(t - \tau_{tar})$$

$$= \sum_{n=0}^{N-1} \mathrm{rect}\left(\frac{t - nT_S - \tau_{tar}}{T_W}\right)e^{j\pi k(t - \tau_{tar})^2},$$

(3)

Finally, the jammer forwards the stored radar signal fragments for M times to generate the resulting jamming signal, which can be expressed as

$$s_{jam}(t) = \sigma_{jam}s_{sam}(t) \otimes \sum_{m=1}^{M} \delta(t - mT_W)$$

$$= \sigma_{jam}\sum_{m=1}^{M}\sum_{n=0}^{N-1} \mathrm{rect}\left(\frac{t - nT_S - mT_W - \tau_{tar}}{T_W}\right)e^{j\pi k(t - mT_W - \tau_{tar})^2},$$

(4)

where σ_{jam} indicates the intensity of the jamming signal.

2.2. PC Result of ISRJ. For LFM radar, the PC process can be regarded as the time-domain convolution between the echo signal and LFM radar matched filter $sig^*(-t)$. For the jamming slice formed by the m th forwarding of the n th sampled signal fragment, the PC result can be formulated as follows:

$$S_{PC}^{m,n}(t) = \sigma_{jam} rect\left(\frac{t - nT_S - mT_W}{T_W}\right)e^{j\pi k\left(t - mT_W\right)^2} \otimes sig^*(-t)$$

$$= \sigma_{jam}\int_{-\infty}^{\infty} rect\left(\frac{\tau - T_W - nT_S}{T_W}\right)rect\left(\frac{t - \tau}{T}\right)\bullet e^{j\pi k\left(\tau - mT_W\right)^2}\bullet e^{-j\pi k(t - \tau)^2}d\tau, \tag{5}$$

$$= \sigma_{jam}T_W sinc\left[kT_W\left(t - mT_W\right)\right]e^{j phase(t)},$$

where $phase(t) = \pi k(t - mT_W)(2nT_S + mT_W - t)$. τ_{tar} is omitted for convenience, which does not affect the derivation result. Equation (5) shows that the PC result of a jamming slice is a "sinc" form function with corresponding

time delay and phase shift. Moreover, for all jamming slices with the m th forwarding time, their PC results can be represented as

$$S_{PC}^m(t) = S_{PC}^{m,0}(t)\sum_{n=0}^{N-1} e^{j2\pi k\left(t - mT_W\right)nT_S}$$

$$= \sigma_{jam}T_W sinc\left[kT_W\left(t - mT_W\right)\right]e^{-j\pi k\left(t - mT_W\right)^2}\frac{1 - e^{j2\pi k\left(t - mT_W\right)NT_S}}{1 - e^{j2\pi k\left(t - mT_W\right)T_S}} \tag{6}$$

$$= \sigma_{jam}T_W sinc\left[kT_W\left(t - mT_W\right)\right]\frac{\sin\left[N\beta_m(t)\right]}{\sin\left[\beta_m(t)\right]}e^{j(N-1)\beta_m(t)}e^{-j\pi k\left(t - mT_W\right)^2},$$

where $\beta_m(t) = \pi k(t - mT_W)T_S$. Therefore, the amplitude response of the whole ISRJ PC result can be expressed as

$$\left|S_{PC}(t)\right| = \sum_{m=1}^{M}\left|S_{PC}^m(t)\right|$$

$$= \sigma_{jam}T_W\sum_{m=1}^{M}\left|sinc\left[kT_W\left(t - mT_W\right)\right]\frac{\sin\left[N\beta_m(t)\right]}{\sin\left[\beta_m(t)\right]}\right|. \tag{7}$$

As depicted by equation (7), it can be seen that ISRJ can generate M false target groups after PC, and different false target groups are formed by the sampled radar signal fragments of different forwarding times. For a particular false target group, when $\beta_m(t) = i\pi, i.e., t = i/kT_S + mT_W, i\epsilon N$, a local peak value can be achieved with $\sin\left[N\beta_m(t)\right]/\sin\left[\beta_m(t)\right] = N$.

In summary, ISRJ can generate multiple false target groups whose amplitude responses are codetermined by T_W, σ_{jam}, N, and M. Among them, T_W, σ_{jam}, and N jointly determine the amplitude peak value. At the same time, T_W also decides the distribution intervals among false target groups. Finally, M determines the number of false target groups.

2.3. TF Analysis of PC Result.

As a joint function of time and frequency, the TF transform can explicitly describe the variation of signal frequency over time and has become an essential tool for analyzing nonstationary signals. In general, linear TF transform is realized by short-time Fourier transform (STFT), which can be expressed as

$$stft(s(t), t, f) = \int_{-\infty}^{\infty} s(t')h(t' - t)e^{-j2\pi ft'}dt', \tag{8}$$

where $s(t)$ is the input signal to be analyzed, and $h(t)$ is a sliding window function.

For the PC results of ISRJ, taking $S_{PC}^{m,n}(t)$ as an example, when a rectangular window is employed, the TF distribution can be formulated as

$$TF_{jam}(\tau, f) = stft\left(S_{PC}^{m,n}(t), \tau, f\right)$$

$$= \sigma_{jam}T_W\int_{-\infty}^{\infty} sinc\left[kT_W\left(t - mT_W\right)\right]e^{j phase(t)}$$

$$\cdot rect\left(\frac{t - \tau}{b}\right)e^{-j2\pi ft}dt, \tag{9}$$

where τ is the sliding time, and b is the sliding window length.

Equation (9) is a Fresnel integral, so an exact analytical solution cannot be derived. An approximation is obtainable through the principle of stationary phase. According to the principle of stationary phase, let the derivative of phase $\varphi(t) = phase(t) - 2\pi ft$ be zero, and we can get that the relationship between time and frequency is

$$t = nT_S + mT_W - f/k. \tag{10}$$

By substituting equation (9) into equation (10), the approximate amplitude response of this integral can be obtained as

$$\left|TF_{jam}(t,f)\right| = \sigma_{jam}T_W sinc\left[kT_W(t - mT_W)\right]$$
$$\cdot sinc\left[T_W(f - nkT_S)\right]. \tag{11}$$

It can be seen from (10) that the TF distribution of a certain ISRJ jamming slice after PC presents the form of "sinc" in the time domain and frequency domain, respectively, and its corresponding positions in these two signal domains separately depend on the interception order n and the forwarding order m of the sampled radar signal fragment. Therefore, the PC result of the whole ISRJ appears as multiple sinc-shaped fluctuations regularly arranged in the TF domain.

Besides ISRJ, the echo signal also contains target echo signals and noise signal $n(t)$, i.e.,

$$s_r(t) = s_{tar}(t) + s_{jam}(t) + n(t), \tag{12}$$

where the TF distributions of the noise signal and target echo signal after PC are easy to learn. The energy of the noise signal scatters evenly throughout the TF domain because the noise signal cannot obtain coherent processing gain in the PC process. In contrast, the energy of the target echo signal after PC concentrates on a specific range gate and distributes uniformly within the bandwidth as a result of linear frequency modulation, presenting a time-unvarying and continuous line in the TF domain.

The TF distribution of the echo signal after PC is shown in Figure 2, which is consistent with the above analysis. In the TF domain, the target echo signal after PC presents a continuous strip distribution, while the false targets present a regular and discontinuous distribution due to the fragment interception and forwarding of ISRJ. Therefore, real targets and false target groups can be well distinguished on the basis of different TF distribution characteristics.

3. The Proposed Method

3.1. Target Identification Based on TF Information Entropy.
Information entropy is an important metric for measuring the uncertainty of the information source, which solves the problem of quantitative measurement of information. We assume that the occurrence probability of each event in an event set S is $P = \{p_1, p_2, \cdots, p_l\}$, where l is the total number of events in S, and $\sum_{e=1}^{l} p_e = 1$. Then, information entropy can be defined as

$$H(S) = -\sum_{e=1}^{l} p_e \log_\alpha p_e, \tag{13}$$

where α is set at 2 in this study.

When the influence of noise is not considered, the instantaneous spectrums of target range gates are shown in Figure 3. For the range gate of the real target, the instantaneous spectrum has the spectrum characteristic of LFM signals. By contrast, for the range gate of the ISRJ false target, in line with the analysis in Section 2.3, the instantaneous spectrum has a regular distribution of sinc-shaped fluctuations, resulting in a lower TFIE. In practice, due to the signal
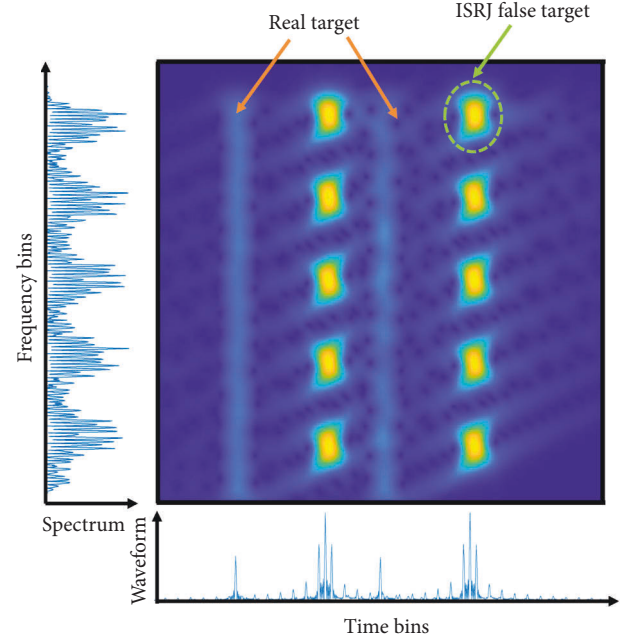

FIGURE 2: The TF distribution of the echo signal after PC. The main graph shows the TF distribution of the PC result, and the corresponding PC result in the time domain and the frequency domain is shown below and to the left of the main graph, respectively. There are two real targets with self-protection jammers, and the intercepted radar signal is forwarded once.

edge effect in the TF transform, the instantaneous spectrums of real targets and ISRJ false targets will affect each other.

In consideration of the different TF distribution characteristics between real targets and ISRJ false targets in the TF domain, this study proposes a target identification method based on TFIE. Specifically, the target range gates can be determined through sparse representation, which has been an emerging signal-processing approach in recent years. Signal sparse representation aims to capture the intrinsic nature of the signal and represent the signal with a few atoms in a given overcomplete dictionary, so as to obtain a more concise representation of the signal, which facilitates further signal processing as well as information acquisition. With the radar-transmitting signal dictionary, the real targets and main false targets can be precisely located due to the energy matching by range gates. After locating the target range gates, features of target instantaneous spectrums can be extracted for target identification. In this study, a support vector machine (SVM), a generalized linear classifier for multivariate classification based on supervised learning, is employed in the target identification process. By learning the data distribution, SVM can determine the decision boundaries among different target groups, thus realizing target distinguishment.

The process of TFIE extraction is as follows:

(1) Transforming the PC result of the echo signal into the TF domain through STFT.

(2) Extracting the instantaneous spectrum F_I of the target range gates according to the sparse representation result $\hat{x}$.
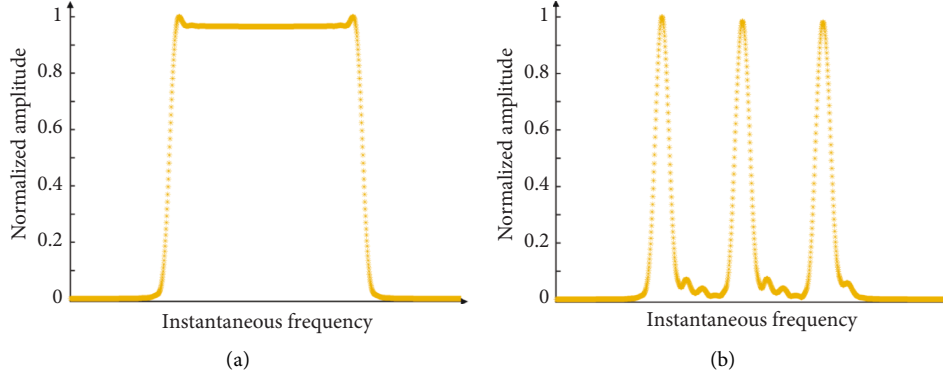
FIGURE 3: The instantaneous spectrums of target range gates. (a) Real target instantaneous spectrum. (b) ISRJ false target instantaneous spectrum.

(3) Guided by the bandwidth B and the center frequency f_m, performing bandwidth normalization on F_I to exclude the effect of noise outside the bandwidth.

(4) Carrying out amplitude normalization, and calculating the probability of each amplitude value within the bandwidth of the normalized instantaneous spectrum F_{NI}, i.e., $P_f = \{p_{f1}, p_{f2}, \cdots, p_{fL}\} = \{/, /, \cdots, /\}$, where $a_{fj}, j \epsilon N$, is the amplitude of each frequency point, A is the total amplitude value, and L is the fixed sampling number of the instantaneous spectrum after bandwidth normalization.

(5) Calculating TFIE values of the corresponding targets using equation (13).

After the above feature extraction steps are completed, the extracted TFIE features are input into an SVM for target identification.

3.2. Sparse Reconstruction of Real Target.

Since ISRJ is generated by fragment interception, storage, and repeated forwarding of radar-transmitting signals, each generated jamming slice can be seen as a radar-transmitting signal with shorter pulse width and different time delay. Therefore, based on the intrapulse coherence of ISRJ, a dictionary of radar-transmitting signals $\Phi \in \mathbb{C}^{N_r \times R_{bin}}$ can be designed to match the echo signal under ISRJ, where N_r is the sampling number in range direction, and R_{bin} is the number of range gates. Hence, the echo signal can be rewritten as

$$s_r(t) = s_{tar}(t) + s_{jam}(t) + n(t) = \Phi * x + n(t), \tag{14}$$

where $\Phi = [\phi_{i,j}]_{N_r \times R_{bin}}$ and the specific element in this dictionary can be represented as

$$\phi_{i,j} = \begin{cases} \text{sig}[(i - j + 1)\Delta t], & j \le i < j + \lfloor T/\Delta t \rfloor, \\ 0, & else, \end{cases} \tag{15}$$

where $\lfloor \bullet \rfloor$ is the round-off operator, and Δt is the sampling interval. It can be seen from equation (15) that each column in Φ is a delayed form of the radar-transmitting signal, and the time interval between two adjacent columns is Δt. Thus, the range resolution of the dictionary can be calculated as $\rho_r = \Delta t \bullet c$.

Sparse representation of the echo signal in nature can be viewed as the coherent matching of targets from different range gates, and $x \in \mathbb{R}^{R_{bin} \times 1}$ represents the matching energy at each range gate. If there are a relatively limited number of significant targets compared with R_{bin} in the imaging scene, the targets can be regarded as sparsely distributed in the range domain. Consequently, x contains only several nonzero values, and the indexes of these nonzero values correspond to the target positions. It is worth noting that the noise signal $n(t)$ cannot obtain the radar processing gain due to its incoherence, resulting in corresponding negligible energy in the sparse domain.

The sparse representation of the echo signal can be realized through the following convex optimization equation:

$$\min_x \left\| s_r(t) - \Phi \bullet x \right\|_2^2 + v \|x\|_1, \tag{16}$$

where $_p$ is the $p-$ norm, and v is a trade-off coefficient to balance the optimization proportion between the sparsity $\|\hat{x}\|_1$ and the residual component $\hat{r} = s_r(t) - \Phi * \hat{x}$. In (15), the larger the v is, the more the $\|\hat{x}\|_1$ is taken into account in the optimization process, and the resulting optimization result $\hat{x}$ is relatively sparser. However, the residual component is larger in this case. On the contrary, there is less residual component left when v is smaller, but the sparsity of the sparse representation result will accordingly decrease. A typical sparse representation result is shown in Figure 4.

As shown in Figure 4, there are many peaks (nonzero values) at the corresponding positions of the real targets and ISRJ false targets because of their matching characteristics with the dictionary Φ, and the peak values of the false targets within the same false target group conform to the modulation of $\sin[N\beta_m(t)]/\sin[\beta_m(t)]$ envelope, which is in consistency with the derivation result of equation (7). Based on the sparse representation result, the obtained target positions can be expressed as

$$r_t = \begin{cases} i, & \hat{x}(i) > \gamma, \\ NaN, & else, \end{cases} \tag{17}$$

$$i = 1, 2, 3, \ldots, R_{bin},$$

where γ is a threshold to distinguish between the range gates with and without targets, and NaN denotes not a number value.
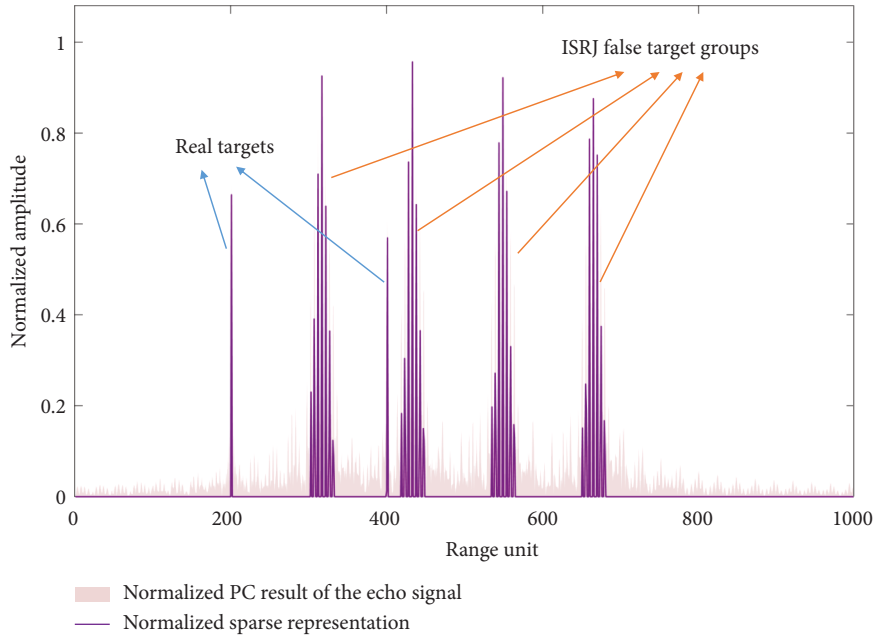
FIGURE 4: Sparse representation of the echo signal. The pink part shows the PC result of the echo signal and the purple line demonstrates the corresponding sparse representation result. In this case, the first real target carries the ISRJ jammer, and there are four false target groups, which means the forwarding time $M = 4$.

With the acquired target positions, TFIE features can be extracted from the instantaneous spectrums for target identification. Assuming that the positions of the identified false targets are r_j in the target identification result i_t, then an adaptive filter can be accordingly constructed in the sparse domain to retain the peaks of real targets and filter out the peaks caused by ISRJ, which can be expressed as

$$F(r) = \begin{cases} 0, & r \in r_j, \\ 1, & \text{else.} \end{cases} \quad (18)$$

Finally, after amplitude compensation, the reconstructed target echo signals can be obtained as

$$\widehat{s}_t = \lambda \Phi \sigma_{\text{opt}} = \lambda \Phi \widehat{x} F, \quad (19)$$

where λ is the amplitude compensation factor, which is the amplitude ratio of the real targets before ISRJ suppression to the corresponding reconstructed targets.

3.3. Main Steps of the Proposed Method. As analyzed in Section 2.3, real targets and ISRJ false targets have different distribution characteristics in the TF domain. Therefore, in view of this inherent difference and to make full use of the coherence of ISRJ, this study proposes a method for ISRJ suppression, which can be mainly divided into three steps: sparse representation, target identification, and real target sparse reconstruction. Firstly, considering the coherence of ISRJ, a dictionary of radar-transmitting signals is designed to represent the echo signal sparsely. Due to the matching with the dictionary, there will be peaks at the corresponding positions of the real targets and the ISRJ false targets in the sparse representation domain. Then, the echo signal is pulse compressed and transformed into the TF domain.

According to the obtained target positions, the TFIE features of the corresponding targets are extracted for target identification. Consequently, only the identified real targets can be retained in the sparse domain to complete target reconstruction. The detailed steps of the proposed method are listed in Algorithm 1.

4. Simulations

4.1. Target Identification Result. In order to verify the effectiveness of TFIE in distinguishing real targets from ISRJ false targets, we set the jamming slice width T_W at $5\,\mu s$, the forwarding time $M = 3$, and the jamming-to-signal ratio (JSR) at $15\,dB$, respectively. Radar transmits LFM signals with bandwidth $B = 9MHz$ and pulse width $T = 60\mu s$. Under these settings, the mean TFIE values of real targets and ISRJ false targets are calculated on different signal-to-noise ratio (SNR) conditions, as shown in Figure 5. Each value is the average result of 500 Monte Carlo simulations.

It can be seen from Figure 5 that the mean TFIE value of real targets is hardly affected by the change of SNR and remains stable at around 8.94, while that of ISRJ false targets decreases slowly as SNR increases, and at length levels off when SNR is greater than 0 dB. From an overall perspective, the mean TFIE value of ISRJ false targets is lower than that of real targets because of the regular TF distribution of ISRJ false targets. In addition, there is no overlap between the curves of real targets and ISRJ false targets, presenting an obvious distinction.

In [32], Yang et al. use the variance feature to detect ISRJ according to the fluctuation of spectrum energy. However, on account of the difference in data dimension and mean value between the variance feature and the TFIE feature, we

Input: The echo signal $s_r(t)$, the sliding window $h(t)$, the trained SVM, the dictionary Φ, and the target locating threshold γ.
Output: Target positions r_t, target identification result i_t, the reconstructed target echo signal $\hat{s}_t$.
Begin
(1) Carry out sparse representation $\hat{x}$ for $s_r(t)$;
(2) Obtain the target positions r_t according to the preset threshold γ;
(3) Perform pulse compression to $s_r(t)$;
(4) Implement STFT to transform the PC result $S_{PC}(t)$ into TF domain;
(5) Extract TFIE features according to the acquired target positions r_t;
(6) Input the TFIE features into the trained SVM and obtain the target identification result i_t;
(7) Construct an adaptive filter F based on i_t;
(8) Perform adaptive filtering in the sparse representation result $\hat{x}$ to retain the corresponding peaks of real targets and filter out the corresponding peaks of the false targets;
(9) Reconstruct the target echo signal $\hat{s}_t$ through Φ and amplitude compensation to obtain the jamming-free result;
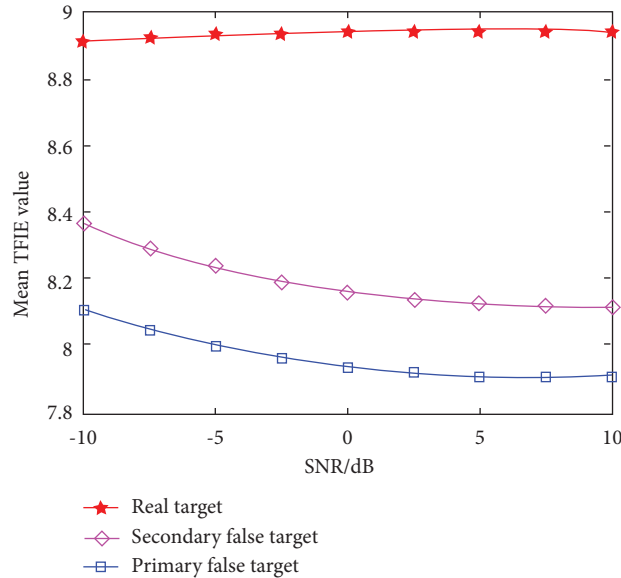**End**

ALGORITHM 1: The proposed method.

FIGURE 5: Mean TFIE value of targets. False targets are further divided into primary targets which are located in the middle of the false target group and other secondary targets.

cannot compare the dispersion degree of these two features directly through standard deviation. Therefore, the coefficient of variation (C.V) is introduced in this study, which is a normalized metric to measure the dispersion degree and can be defined as the ratio of standard deviation σ to mean value μ, i.e.,

$$C.V = \frac{\sigma}{\mu}. \tag{20}$$

As a dimensionless quantity, C.V is a better metric to compare the stability among data groups with different dimensions or mean values, as it eliminates the effect brought by various data values. Specifically, the C.V values of these two features are separately calculated by 500 Monte Carlo simulations under each SNR scenario. As demonstrated in Figure 6, both features of targets tend to be more stable with the increase of SNR. But on the whole, the C.V of the TFIE feature is remarkably smaller than that of the

variance feature, indicating that the TFIE feature is less discrete and possesses better stability.

The proposed method in this study transforms the jamming suppression problem into a binary classification problem for targets. ISRJ suppression can be achieved by adaptive filtering based on the identification result. Therefore, the performance of the proposed method depends directly on the target identification accuracy, which can be expressed as

$$P_A = \frac{T_c}{T_t}, \tag{21}$$

where T_t is the total target number, and T_c represents the number of targets correctly identified.

In the supervised learning process, 4000 sets of TFIE features, including 2000 real target features and 2000 ISRJ false target features (with different orders), are generated under different parameter settings, and they are further
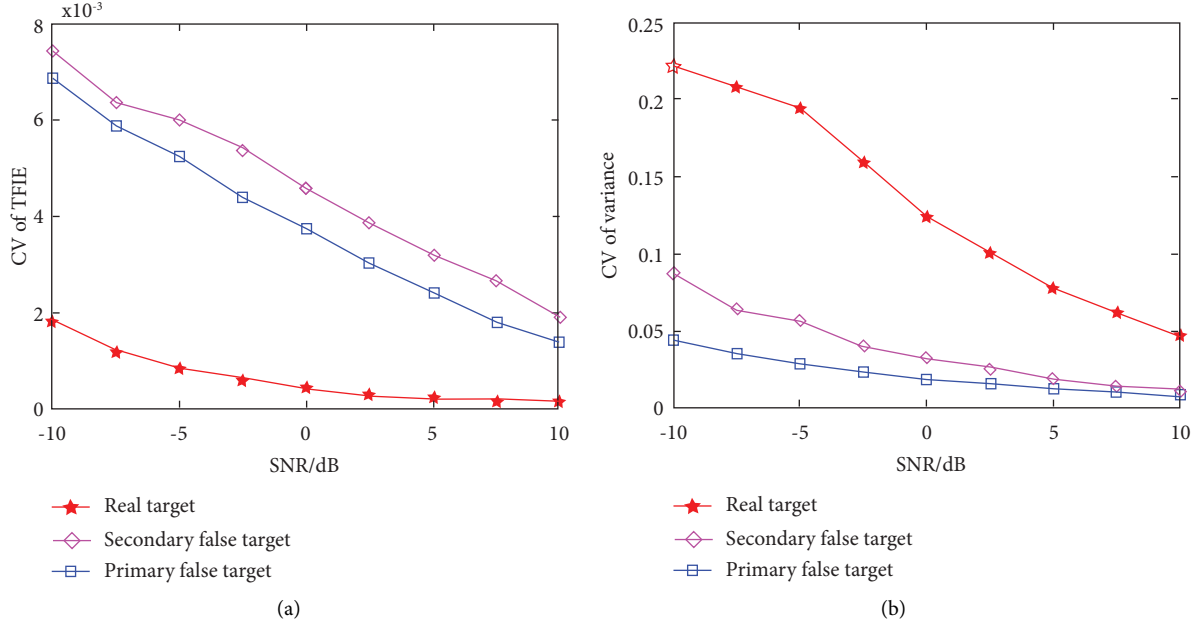
FIGURE 6: C.V of TFIE and variance. (a) TFIE. (b) Variance.

divided into the training set and test set by the ratio of $4:1$. The parameter ranges of training samples are listed in Table 1. After several rounds of data generation and training in accordance with the above settings, the average P_A based on TFIE can reach 99.46%.

The hypothesis test is usually applied to test the robustness of certain conclusions [38]. To further prove the superiority of TFIE in the task of target identification, a one-tailed t-test is carried out in this study, in which P_A serves as the evaluation metric. For the generated datasets, the average test P_A value using TFIE is $\mu_0 = (1/m_1) \sum_{s=1}^{m_1} \hat{\varepsilon}_s = 0.9217$, and the variance is $\sigma_0^2 = [1/(m_1 - 1)] \sum_{s=1}^{m_1} (\hat{\varepsilon}_s - \mu_0)^2 = 1.9167 \times 10^{-5} (m_1 = 6)$. Subsequently, the critical value τ_t can be obtained by $\tau_t = \sqrt{m_1} |\mu_0 - \varepsilon_0|/\sigma_0^2 = 4.347$ (where $\varepsilon_0 = 0.99$ is the assumed minimum P_A value) and is larger than the 4.032 given by the one-tailed t-test table. This result means that the P_A using the TFIE feature is greater than the assumed test P_A value (0.99) at a confidence level of $(1 - \alpha = 0.995)$.

In contrast, we also perform a hypothesis t-test on the variance feature with the same datasets, and the intermediate results of the statistical calculation process are listed in Table 2. The TFIE feature can contribute to a higher P_A with stronger robustness compared with the variance feature.

4.2. Factors Affecting Target Identification Accuracy.
As previously mentioned in Section 3.1, TF features may be affected by the interactions among targets resulting from the signal edge effect in the TF transform. Therefore, some key parameters such as T_W, σ_{jam} (JSR), SNR, N, and M may have an impact on the target identification result. In this section, extensive experiments are done to explore the effect of these key parameters on P_A.

As can be learned from equation (7), the forwarding time M decides the number of false target groups. In other words,

TABLE 1: Parameter ranges of training samples.

Parameter	Value
Sampling frequency f_s/MHz	20
Pulse width T/μs	$50 - 70$
Bandwidth B/MHz	$6 - 10$
Sampling slice width T_W/μs	$(1/15 - 1/10) T$
Forwarding time M	$\{1, 2, 3, 4\}$
Signal-to-noise ratio SNR/dB	$-10 - 10$
Jamming-to-signal ratio JSR/dB	$5 - 20$

TABLE 2: Hypothesis test of the proposed TFIE feature and the variance feature on the generated dataset.

Statistical parameter	TFIE	Variance
μ_0	0.9946	0.9860
ε_0	0.99	0.9788
σ_0^2	6.667×10^{-6}	2.589×10^{-5}
τ_t	4.347	3.509
$1 - \alpha$	0.995	0.99

M merely decides how far the false targets are distributed in the range domain and is unrelated to target intensity, so it can hardly affect P_A. To substantiate this claim, we fix the experimental parameters for the purpose of controlling variables, as shown in Table 3 (for convenience, if not specifically specified, the basic experimental parameters remain unchanged as those in Table 3 in the following simulations). Also, we set the sampling slice width T_W uniformly distributed within the range of $(T/13, T/11)$ so that N remains at 3. Then, two datasets with 10000 features are generated when the forwarding time M is 4 and 5, respectively. The result demonstrates that the P_A values of both datasets are 0.9903, thus indicating that M basically has no direct effect on P_A.

TABLE 3: Basic parameter settings.

Parameter	Value
Sampling frequency f_s/MHz	20
Pulse width T/μs	60
Bandwidth B/MHz	8
Signal-to-noise ratio SNR/dB	−10
Jamming-to-signal ratio JSR/dB	20

TABLE 4: The settings of four generated modes.

Mode no.	Forwarding time M	Sampled fragment number N	Duty ratio (%)
1	1	7	50
2	2	5	33
3	3	4	25
4	4	3	20

In order to study the effect of JSR, SNR, and sampled fragment number N on the target identification accuracy P_A, a series of Monte Carlo experiments are carried out in this study. As for the parameter settings, under the condition that the sampling slice width $T_W = T/14$, test datasets under four modes are generated, as shown in Table 4. In each mode, the test datasets are generated from −10 dB to 10 dB with a 2.5 dB SNR interval and from 5 dB to 20 dB with a 1.5 dB JSR interval, respectively. This results in a total of 99 test datasets per mode and 100 Monte Carlo experiments are conducted in each dataset.

The variation trends of P_A versus SNR and JSR in different jamming modes are illustrated in Figure 7. Simultaneously, the misidentified real targets and false targets are separately counted, and the number distribution versus JSR is shown in Figure 8.

Some key conclusions can be drawn from Figures 7 and 8, which are summarized in the following:

(1) When the signal fragment is forwarded immediately after being intercepted, i.e., $M = 1$, the jamming signal at this time is called interrupted-sampling direct jamming (ISDJ), which differs from ISRJ only in the forwarding time. The Monte Carlo experiment results shown in Figure 7 demonstrate that the proposed method can maintain high levels of P_A in these four modes, which means that the proposed method can effectively counter both kinds of jamming signals.

(2) According to equation (7), the peak amplitudes of the generated false targets become larger with larger N, which is unfavorable for the correct identification of real targets as they are more likely to be covered by ISRJ false target groups. On the other hand, as analyzed in Section 2.2, false targets are generated at the interval of $1/kT_S$ within a false target group, so a broader jamming area is yielded when N becomes larger (T_S is smaller accordingly), exacerbating the overlapping between real targets and false targets. The above two factors lead to an overall lower P_A.

(3) When JSR is fixed, P_A generally rises with the growth of SNR.

(4) In the case of low JSR, false targets are relatively weak, and their TF features are more affected than the real target features by the mutual effect among targets. In consequence, the primary cause of identification error in this circumstance is ISRJ false targets, and the error rate drops gradually with the increase of JSR.

(5) The same rule applies to real targets in the case of high JSR. Compared with false target features, the TF features of real targets suffer considerably more from the mutual effect among targets. As a result, the misidentified samples mainly come from real targets, and the target identification accuracy P_A falls as JSR increases.

According to equation (6), T_W not only determines the intensity of the ISRJ false target group but also decides the distribution intervals among targets. In order to learn the specific influence of T_W on P_A, two test datasets, including 2000 target features (1000 real target features and 1000 ISRJ false target features), are generated under the conditions of $M = 2$ and $M = 5$, respectively. Correspondingly, T_W is uniformly distributed in the interval of $T_W \in (1/15, 1/13)T$ and $T_W \in (1/15, 1/11)T$ for controlling variables (N remains constant). The misidentified data is statistically analyzed, and the statistical T_W distributions are shown in Figure 9.

Through statistical histograms, the error probability of target identification is seen to fall steadily with the increase of T_W after a sharp rise at first. In terms of the upward trend, the target distribution interval is relatively small, and the mutual effect among targets cannot be ignored. At this time, the intensity of the false target group becomes stronger as T_W increases, so the TF features of the real targets are prone to be affected, bringing about more misidentified real targets. However, when T_W grows to a certain degree, the target distribution interval is large enough to significantly weaken the interactions among targets. Consequently, the error rate starts to decline in general.

4.3. The Jamming Suppression Performance of the Proposed Method. On the ground of an overall high target identification accuracy, the jamming suppression performance of the proposed method is tested. We set three real targets at 1.5 km, 3 km, and 5 km, respectively. The sampling slice width T_W is fixed at 5 μs, and the intercepted radar signal fragments are forwarded three times. The ISRJ jammer is implemented on the real target at 1.5 km to cover all these three targets.

As shown in Figure 10, under the influence of ISRJ, the real targets are mixed with multiple false target groups in the range direction after PC, leading to the inability of radar systems to acquire effective information on real targets. By sparse representation, the positions of targets are obtained so that the TFIE features of targets can be extracted for the subsequent target identification procedure.

With the target identification result, an adaptive filter can be constructed in the sparse domain by equation (18) to
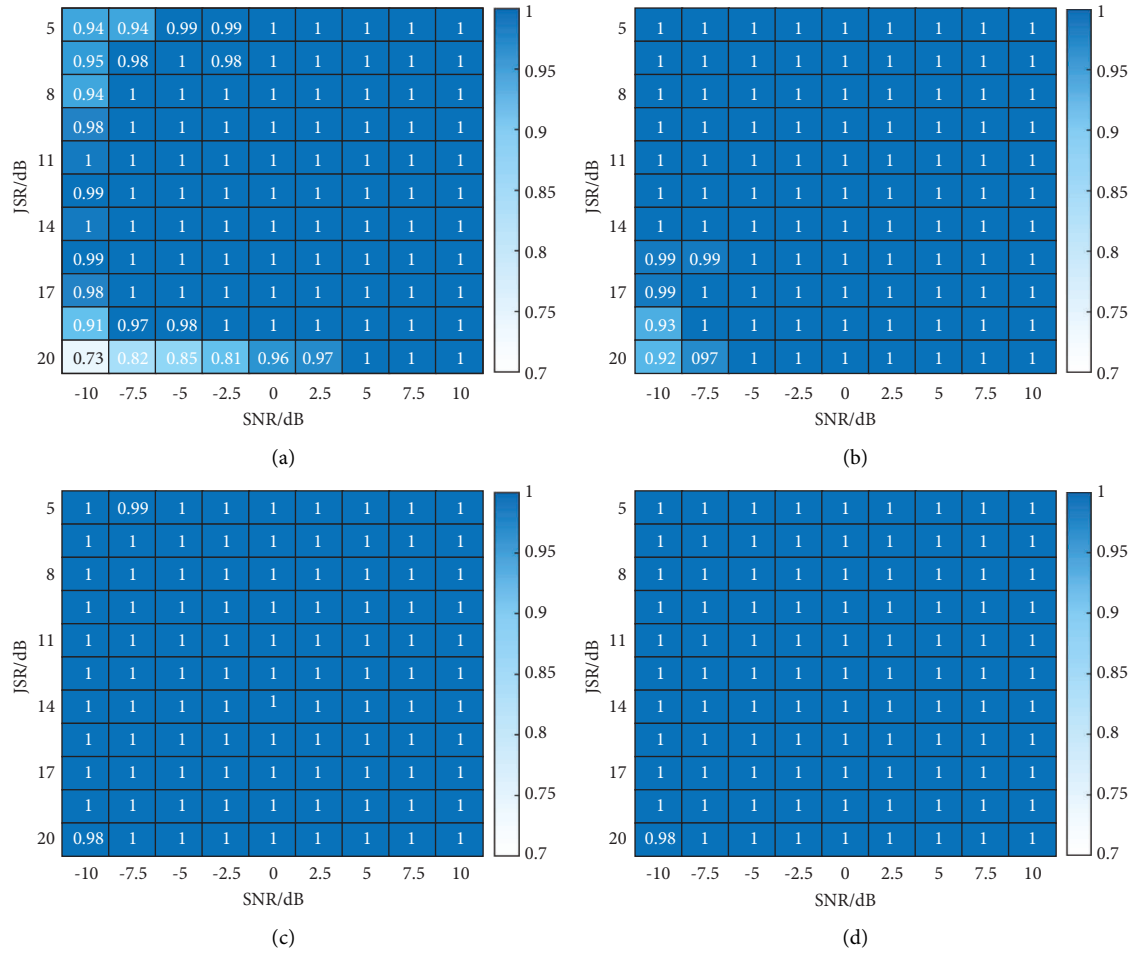
Figure 7: P_A versus SNR and JSR. (a) Mode 1. (b) Mode 2. (c) Mode 3. (d) Mode 4.
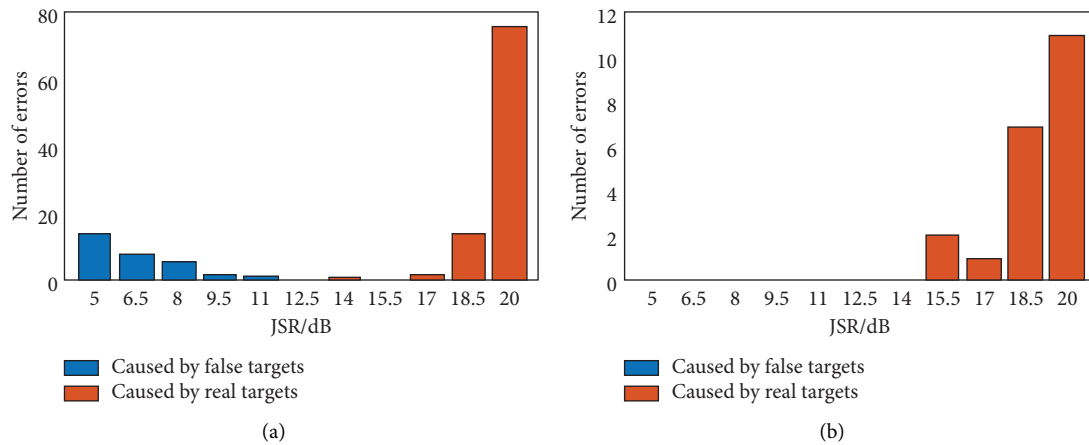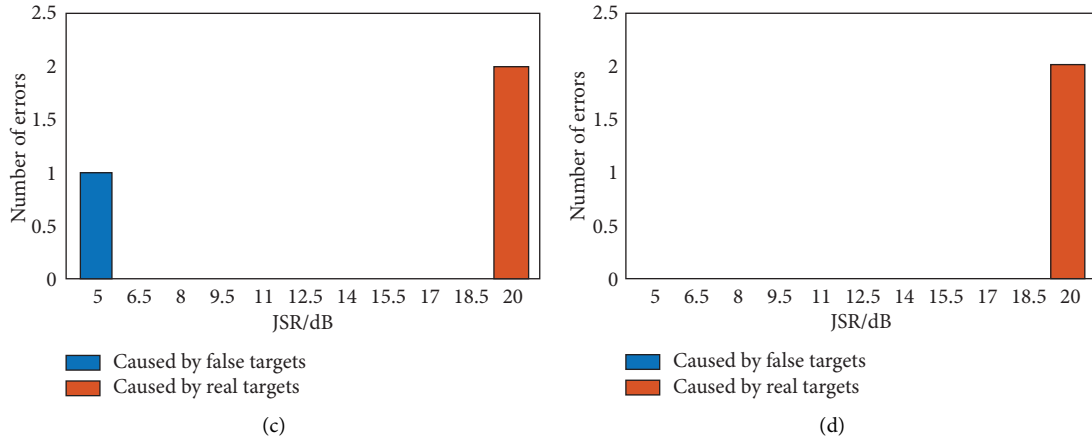

Figure 8: Continued.

(c)

(d)

Figure 8: Misidentified target distribution over JSR. (a) Mode 1. (b) Mode 2. (c) Mode 3. (d) Mode 4.
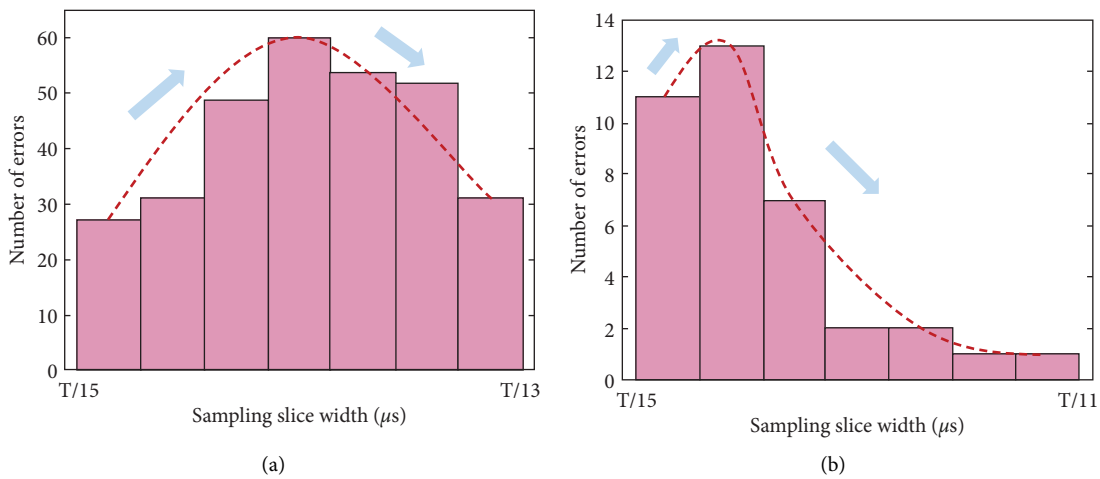

(a)

(b)

Figure 9: T_W distribution of error samples. (a) $M = 2$. (b) $M = 5$.

remove the corresponding peaks of ISRJ false targets. After amplitude compensation, the final jamming suppression result is obtained, as shown in Figure 11. It can be seen that based on the correct target identification result, all the ISRJ false targets are filtered out, and only the real targets are reconstructed. Moreover, the noise signal in the original echo signal is also suppressed to a significant extent since its energy cannot match with the dictionary in the process of sparse representation.

Furthermore, when the real targets and the generated false targets are aliasing in the range direction, which is also a typical scene in common practice, the jamming suppression performance of the proposed method still needs to be tested. Concerning this issue, we set the real target at 3.5 km from the reference point, and the intercepted radar signal is forwarded once to form ISRJ. 4000 sets of target TFIE features are generated with T_W ranging uniformly from 1–30 μs to ensure the real target is aliasing in the different positions (from the middle to the edge) of the false target

group, and the training range of SNR and JSR is in line with Table 1.

Although the mutual effect among targets brought by the signal edge effect in the TF transform cannot be ignored at this time, the overall target identification accuracy P_A still reaches 90.0% in this case, which proves the validity of the proposed method in the target aliasing situation. When the sampling slice width $T_W = 2.5 \mu s$, the corresponding sparse representation and ISRJ suppression results are shown in Figures 12 and 13, respectively.

In practice, another frequently encountered scenario is that the generated ISRJ false target is located ahead of the real target, which can be achieved by frequency shifting [22]. Similarly, 4000 sets of target TFIE features are generated with the sampling slice width T_W set as 4 μs and frequency shift f_d ranging from 0.54 MHz to 1.92 MHz to produce false targets preceding the real target. This range also keeps the real target aliasing in the different positions (from the middle to the edge) of the false target group (if not aliasing,
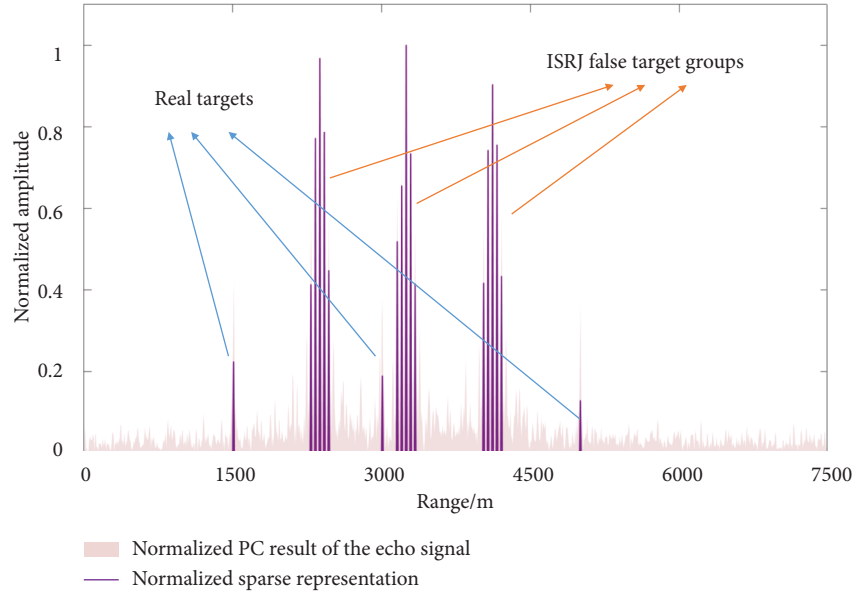
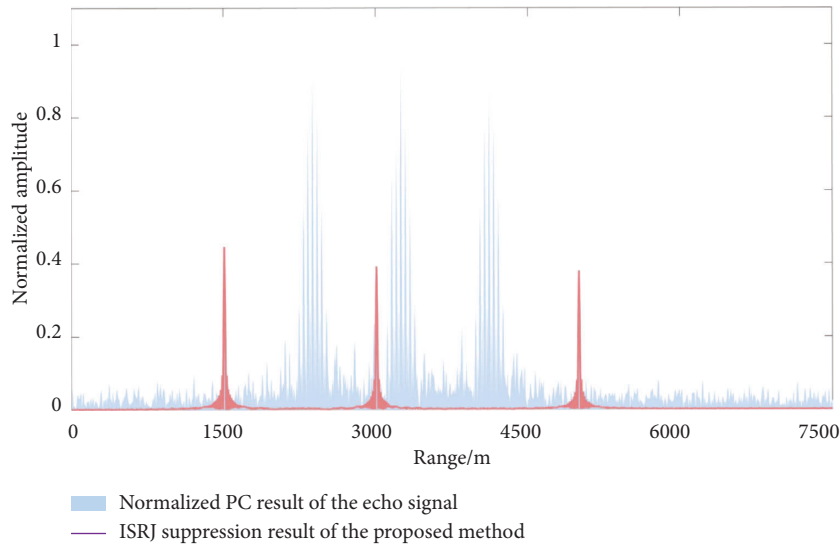FIGURE 10: Spare representation of the echo signal.

FIGURE 11: ISRJ suppression result of the proposed method.

there is no difference from the regular case). Other training parameters remain unchanged. Under this circumstance, the overall P_A is 86.0%, demonstrating the effectiveness of the proposed method in the frequency-shifting situation. The decline in P_A is caused by frequency shifting, which lowers the regularity of the false target instantaneous spectrums and reduces the feature difference between the real targets and ISRJ false targets. When the frequency shift f_d is 1.2 MHz, the corresponding sparse representation and ISRJ suppression results are shown in Figures 14 and 15, respectively.

In order to evaluate the jamming suppression performance quantitatively, the signal-to-jamming ratio improvement factor (SJRIF) is introduced in this study, which is defined as the difference between the signal-to-jamming ratio (SJR) after and before ISRJ suppression, i.e.,

$$SJRIF = SJR_{\text{after}} - SJR_{\text{before}}. \tag{22}$$
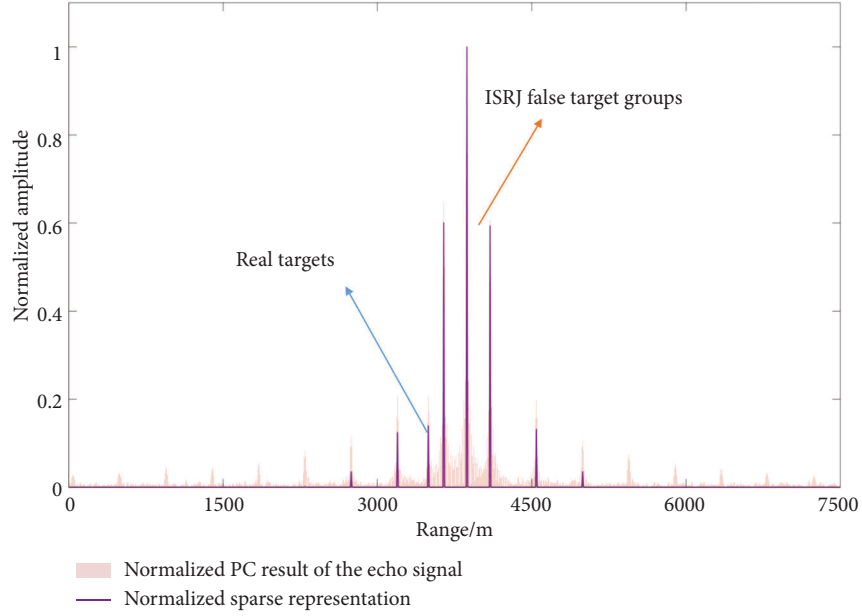
In (21), SJR can be formulated as

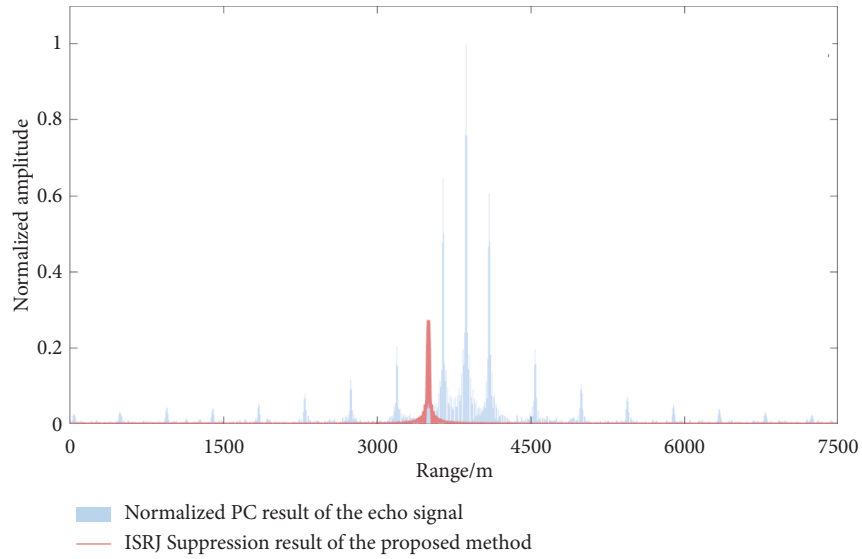FIGURE 12: Spare representation of the echo signal in the target aliasing situation.

FIGURE 13: ISRJ suppression results in the target aliasing situation.

$$SJR = \frac{1}{I} \sum_{i=1}^{I} 20 \log_{10} \left(a_i/a_j \right), \qquad (23)$$

where I denotes the total number of real targets, a_i is the peak amplitude of the ith real target, and a_j is the maximum amplitude besides the real targets.

Monte Carlo simulations are conducted in this study to compare the jamming suppression performance of the proposed method with two typical competing methods proposed in [33, 36]. The simulations are carried out from −10 dB to 10 dB at 5 dB SNR intervals in the low JSR and high JSR scenarios, respectively. Each result is the averaged result of 500 Monte Carlo simulations, which is displayed in Figure 16.
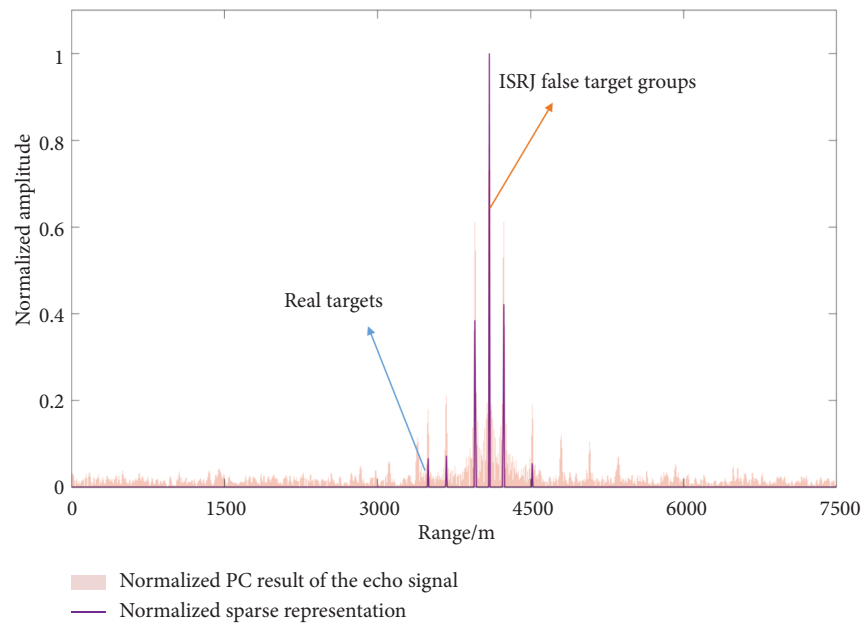
Figure 14: Spare representation of the echo signal in the frequency shifting situation.
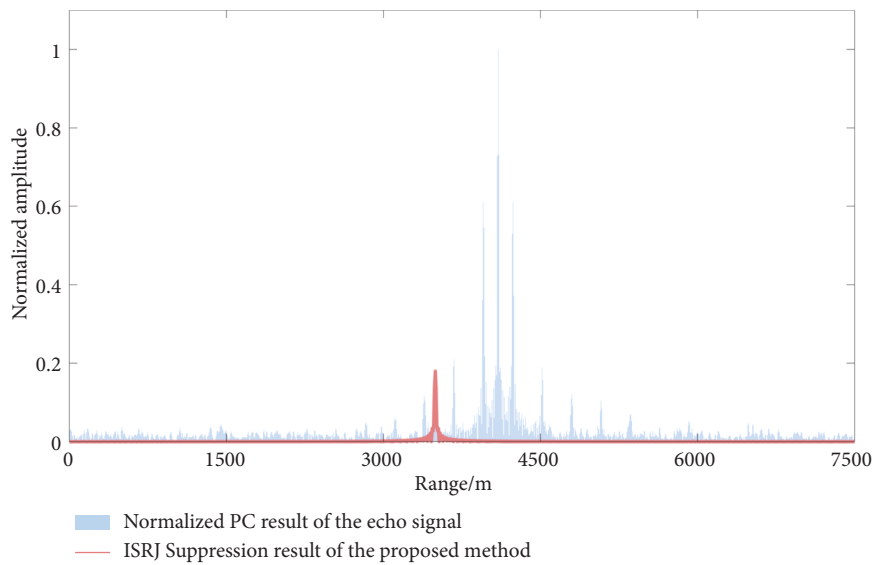

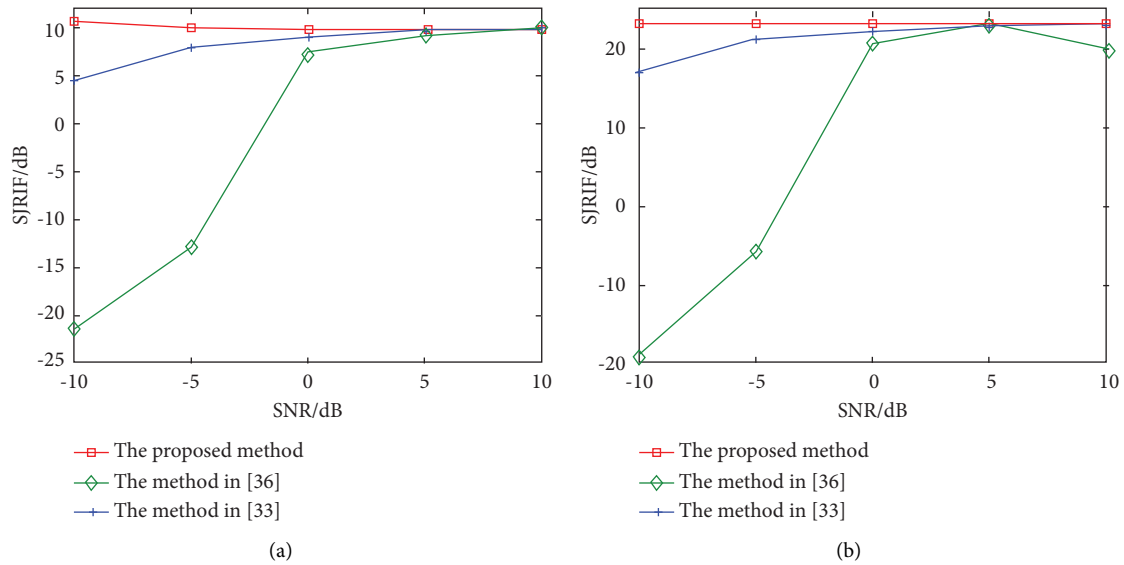Figure 15: ISRJ suppression result in the frequency shifting situation.

Figure 16: JSRIF variation versus SNR. (a) JSR = 5 dB. (b) JSR = 20 dB.

It can be seen from Figure 16 that the method in [36] is prone to be affected by low SNR situations, while the proposed method outperforms the other two methods for PC radars both in high and low JSR situations, demonstrating its superiority against ISRJ.

5. Conclusions

ISRJ is a promising intrapulse coherent jamming that regularly intercepts and retransmits radar-transmitting signals by fragments, resulting in noticeable TF distribution differences between ISRJ false targets and real targets. Given these characteristics, this study proposes a new ISRJ suppression method based on TF analysis and real target sparse reconstruction. The proposed method innovatively converts jamming suppression into a target binary classification problem. Firstly, the echo signal is sparsely represented to obtain the target positions. Then, guided by the previously acquired positions, the target features are extracted in the TF domain for subsequent target identification. In the end, the real targets are reconstructed according to the target identification result, thus realizing ISRJ suppression.

Simulation experiments are conducted to validate the effectiveness of the proposed method under various situations, and the factors that may affect the target identification accuracy are also studied in detail. In the scheme of target identification, hypothesis tests reveal that the adopted TFIE feature can achieve improved performance than the variance feature, with an overall target identification accuracy of 99.46%. As for the final ISRJ suppression result, only the real targets are retained and reconstructed, while the false ISRJ targets and the noise signal are suppressed considerably. Through quantitative evaluation, the proposed method shows better performance than competing methods for pulse compression radar.

Data Availability

The simulation data used to support the findings of this study are available from the corresponding author upon reasonable request.

Conflicts of Interest

The authors declare that there are no conflicts of interest regarding the publication of this paper.

Acknowledgments

References

[1] S. Baher Safa Hanbali, "Technique to counter improved active echo cancellation based on ISRJ with frequency shifting," *IEEE Sensors Journal*, vol. 19, no. 20, pp. 9194–9199, 2019.

[2] D. C. Schleher, *Electronic Warfare in the Information Age*, Artech House, Boston, MA, USA, 1999.

[3] S. D. Berger, "Digital radio frequency memory linear range gate stealer spectrum," *IEEE Transactions on Aerospace and Electronic Systems*, vol. 39, no. 2, pp. 725–735, 2003.

[4] G. Liu, K. Zheng, and M. Gao, "Design and implementation of deception jamming signal generator against SAR," *Transactions of Beijing Institute of Technology*, vol. 32, no. 2, pp. 184–188, 2012.

[5] A. Almslmany, C. Wang, and Q. Cao, "Advanced deceptive jamming model based on DRFM Sub-Nyquist sampling," in *Proceedings of the 2016 13th International Bhurban Conference on Applied Sciences and Technology (IBCAST)*, pp. 727–730, Islamabad, Pakistan, January 2016.

[6] M. Greco, F. Gini, and A. Farina, "Radar detection and classification of jamming signals belonging to a cone class," *IEEE Transactions on Signal Processing*, vol. 56, no. 5, pp. 1984–1993, 2008.

[7] J. Akhtar, "Orthogonal block coded ECCM schemes against repeat radar jammers," *IEEE Transactions on Aerospace and Electronic Systems*, vol. 45, no. 3, pp. 1218–1226, 2009.

[8] J. Zhang, Y. Li, and X. Zhu, "Approach of radar against deception jamming based on waveform diversity," *Journal of Data Acquisition & Processing*, vol. 25, no. 2, pp. 138–142, 2010.

[9] Y. Li, X. Jia, Y. Chen, and C. Yin, "Frequency agility MIMO-SAR imaging and anti-deception jamming performance," in *Proceedings of the 2014 XXXIth URSI General Assembly and Scientific Symposium (URSI GASS)*, pp. 1–4, Beijing, China, August 2014.

[10] N. Levanon, "Stepped-frequency pulse-train radar signal," *IEE Proceedings - Radar, Sonar and Navigation*, vol. 149, no. 6, pp. 297–309, 2002.

[11] S. Jin, C. Wang, C. Qiu, and X. Li, "Design of RF protecting signal for transponder jamming suppression," *Journal of China Academy of Electronics and Information Technology*, vol. 9, no. 4, pp. 377–381, 2014.

[12] Z. Sun, M. Dong, and B. Chen, "Interrupted sampling repeater jamming suppression based on time-frequency analysis and band-pass filtering," *Journal of Xidian University*, vol. 48, no. 2, pp. 139–146+180, 2021.

[13] X. Wang, J. Liu, W. Zhang, Q. Fu, Z. Liu, and X. Xie, "Mathematic principles of interrupted-sampling repeater jamming (ISRJ)," *Science in China - Series F: Information Sciences*, vol. 50, no. 1, pp. 113–123, 2007.

[14] D. Feng, L. Xu, X. Pan, and X. Wang, "Jamming wideband radar using interrupted-sampling repeater," *IEEE Transactions on Aerospace and Electronic Systems*, vol. 53, no. 3, pp. 1341–1354, 2017.

[15] D. Feng, H. Tao, Y. Yang, and Z. Liu, "Jamming de-chirping radar using interrupted-sampling repeater," *Science China Information Sciences*, vol. 54, no. 10, pp. 2138–2146, 2011.

[16] X. Pan, W. Wang, D. Feng, Y. Liu, Q. Fu, and G. Wang, "On deception jamming for countering bistatic ISAR based on sub-Nyquist sampling," *IET Radar, Sonar & Navigation*, vol. 8, no. 3, pp. 173–179, 2014.

[17] X. Pan, W. Wang, Q. Fu, D. Feng, and G. Wang, "Simulation of two-dimensional ISAR decoys on a moving platform," *Journal of Systems Engineering and Electronics*, vol. 26, no. 2, pp. 250–257, 2015.

[18] Q. Wu, F. Zhao, X. Ai, X. Liu, and S. Xiao, "Two-dimensional blanket jamming against ISAR using nonperiodic ISRJ," *IEEE Sensors Journal*, vol. 19, no. 11, pp. 4031–4038, 2019.

[19] H. Li, G. Zheng, Y. Yang, and H. Guo, "The performance analysis of multi-false targets jamming of part copying radar pulse," *Electronic Information Warfare Technology*, vol. 25, no. 3, pp. 39–44, 2010.

[20] Z. Liu, "Jamming technique for countering LFM pulse compression radar based on digital radio frequency memory," *Doctoral Thesis*, National University of Defense Technology, China, 2006.

[21] W. Yang, J. Lin, and T. Wang, "Intermittent sampling scatter-wave jamming against SAR," *Journal of Astronautics*, vol. 3, no. 33, pp. 367–373, 2012.

[22] C. Li, W. Su, G. Hong, C. Ma, and J. Chen, "Improved interrupted sampling repeater jamming based on DRFM," in *Proceedings of the 2014 IEEE International Conference on Signal Processing, Communications and Computing (ICSPCC)*, pp. 254–257, Guilin, China, August 2014.

[23] J. Zhang, H. Mu, S. Wen, and Y. Li, "Anti interrupted-sampling repeater jamming method based on stepped LFM waveform," *Systems Engineering and Electronics*, vol. 41, no. 5, pp. 1013–1020, 2019.

[24] J. Zhang, H. Mu, S. Wen, S. Liao, and M. Sha, "Anti-intermittent sampling jamming method based on intra-pulse LFM-Costas frequency stepping," *Systems Engineering and Electronics*, vol. 41, no. 10, pp. 2170–2177, 2019.

[25] J. Zhang and C. Zhou, "Interrupted sampling repeater jamming suppression method based on hybrid modulated radar signal," in *Proceedings of the 2019 IEEE International Conference on Signal, Information and Data Processing (ICSIDP)*, pp. 1–4, Chongqing, China, December 2019.

[26] C. Zhou, F. Liu, and Q. Liu, "An adaptive transmitting scheme for interrupted sampling repeater jamming suppression," *Sensors*, vol. 17, no. 11, p. 2480, 2017.

[27] H. Yuan, C. y. Wang, X. Li, and L. An, "A method against interrupted-sampling repeater jamming based on energy function detection and band-pass filtering," *International Journal of Antennas and Propagation*, vol. 2017, no. 1, pp. 1–9, 2017.

[28] H. Yuan, C. Wang, X. Li, and L. An, "ECCM scheme against interrupted-sampling repeater jamming based on compressed sensing signal reconstruction," *Systems Engineering and Electronics*, vol. 40, no. 4, pp. 717–725, 2018.

[29] J. Chen, W. Wu, S. Xu, Z. Chen, and J. Zou, "Band pass filter design against interrupted-sampling repeater jamming based on time-frequency analysis," *IET Radar, Sonar & Navigation*, vol. 13, no. 10, pp. 1646–1654, 2019.

[30] J. Chen, S. Xu, J. Zou, and Z. Chen, "Interrupted-sampling repeater jamming suppression based on stacked bidirectional gated recurrent unit network and infinite training," *IEEE Access*, vol. 7, pp. 107428–107437, 2019.

[31] S. Gong, X. Wei, and X. Li, "ECCM scheme against interrupted sampling repeater jammer based on time-frequency analysis," *Journal of Systems Engineering and Electronics*, vol. 25, no. 6, pp. 996–1003, 2014.

[32] S. Yang, B. Tian, and R. Zhou, "ECCM against interrupted sampling repeater jamming based on time-frequency analysis," *Journal of Signal Processing*, vol. 32, no. 10, pp. 1244–1251, 2016.

[33] C. Zhou, Q. Liu, and X. Chen, "Parameter estimation and suppression for DRFM based interrupted sampling repeater jammer," *IET Radar, Sonar & Navigation*, vol. 12, no. 1, pp. 56–63, 2018.

[34] Y. Meng, L. Yu, Y. Wei, and P. Tong, "A novel parameter estimation method of interrupted sampling repeater jamming," in *Proceedings of the 2019 IEEE International Conference on Signal, Information and Data Processing (ICSIDP)*, pp. 1–5, Chongqing, China, December 2019.

[35] X. Lu, J. Yang, C. Ma, H. Gu, and W. Su, "Wide-band interference mitigation algorithm for SAR based on time-varying filtering and sparse recovery," *Electronics Letters*, vol. 54, no. 3, pp. 165–167, 2018.

[36] C. Zhou, Q. Liu, and C. Hu, "Time-frequency analysis techniques for recognition and suppression of interrupted sampling repeater jamming," *Journal of Radars*, vol. 8, no. 1, pp. 100–106, 2019.

[37] Z. Wang, W. Yu, Z. Yu, Y. Luo, and J. Li, "Neural network-guided sparse recovery for interrupted-sampling repeater jamming suppression," *International Journal of Antennas and Propagation*, vol. 2021, pp. 1–13, Article ID 5368600, 2021.

[38] J. Hu and W. Zheng, "A deep learning model to effectively capture mutation information in multivariate time series prediction," *Knowledge-Based Systems*, vol. 203, Article ID 106139, 2020.